DTU Library

On the validity of numerical models for viscothermal losses in structural optimization for micro-acoustics

Andersen, Peter Risby; Cutanda Henriquez, Vicente; Aage, Niels

Published in:
Journal of Sound and Vibration

Link to article, DOI:
10.1016/j.jsv.2022.117455

Publication date:
2022

Document Version
Publisher's PDF, also known as Version of record

Journal of Sound and Vibration 547 (2023) 117455

Contents lists available at ScienceDirect

Journal of Sound and Vibration

journal homepage: www.elsevier.com/locate/jsvi

On the validity of numerical models for viscothermal losses in structural optimization for micro-acoustics

Peter Risby Andersen [a,b,*], Vicente Cutanda Henríquez [a,b], Niels Aage [a,c]

[a] Centre for Acoustic-Mechanical Micro Systems, Technical University of Denmark, Ørsteds Plads, Building 352, DK-2800, Kgs. Lyngby, Denmark
[b] Department of Electrical and Photonics Engineering, Technical University of Denmark, Ørsteds Plads, Building 352, DK-2800, Kgs. Lyngby, Denmark
[c] Department of Civil and Mechanical Engineering, Technical University of Denmark, Ørsteds Plads, Building 352, DK-2800, Kgs. Lyngby, Denmark

ARTICLE INFO

Keywords:
Acoustics
Shape optimization
Adjoint sensitivities
Viscothermal losses
Boundary element method

ABSTRACT

The increasing interest in miniaturizing acoustic devices has made accurate and efficient models of acoustic viscous and thermal losses progressively more important. This is especially the case in micro-acoustic devices such as hearing aids, condenser microphones and MEMS devices. Using the full linearized Navier Stokes equations to numerically model losses comes at a high computational cost. An approximate boundary layer impedance boundary condition representing acoustic losses has therefore become popular due to its high computational efficiency. This is especially true in the context of optimization where an efficient numerical method is required due to the many repeated analyses needed. However, the boundary layer impedance is only valid in the computational region where boundary layers are non-overlapping. Applying the boundary layer impedance can therefore lead to poor optimization results or limit the possible design space if the optimization violates this limitation. Therefore, the benefit of losses in narrow regions cannot be exploited if the boundary layer impedance is used. This work investigates two shape optimization test cases for maximizing the absorption properties of Helmholtz-like geometries based on the Boundary Element Method. The test cases are used to compare and validate the boundary layer impedance against a full viscothermal implementation revealing the benefits of the boundary layer impedance but also its limitations in a structural optimization setting. Based on the numerical experiments it is recommend to avoid the use of the boundary layer impedance in cases where any theoretical boundary layer overlap exists or at least verify simulation and optimization results with a full-losses implementation.

1. Introduction

The interest in modeling of acoustic viscous and thermal losses dates back to the early work by Kirchhoff and Rayleigh [1,2]. Today, numerical modeling of acoustic losses is an essential part of the design process when improving micro-acoustic devices such as hearing aids, condenser microphones and acoustic MEMS devices [3–8]. The importance of losses can also be found in the area of acoustic metamaterials [9,10], but also within room acoustics e.g. when characterizing perforated panels [11].

* Corresponding author at: Centre for Acoustic-Mechanical Micro Systems, Technical University of Denmark, Ørsteds Plads, Building 352, DK-2800, Kgs. Lyngby, Denmark.
E-mail addresses: prandersen@jabra.com (P.R. Andersen), vcuhe@dtu.dk (V.C. Henríquez), naage@dtu.dk (N. Aage).

https://doi.org/10.1016/j.jsv.2022.117455
Received 13 October 2021; Received in revised form 11 October 2022; Accepted 20 November 2022
Available online 30 November 2022

Historically, losses are modeled using the full linearized Navier–Stokes (FLNS) equations using e.g. the Finite Element Method (FEM). Solving the FLNS comes at a significant computational cost compared to the isentropic wave equation. A FEM implementation of the FLNS will add more degrees of freedom (temperature and velocity) to the system of equations and require special boundary layer meshing to capture the boundary layer effects. The FLNS can also be discretized using the Boundary Element Method (BEM). This is typically achieved by applying the Kirchhoff decomposition (KD) [12,13]. The KD implementation using BEM (hereafter referred to as the KD-BEM) has some advantages, e.g boundary layer meshing is avoided and it is only necessary to solve for surface variables. However, it is cumbersome to implement and will at least contain some dense regions in the final system of equations. On the other hand, it has been shown that some of the dense matrix contributions can be circumvented using a truncation of the viscous and thermal integration kernels (see Andersen et al. 2019 [14] Appendix A).

An approximate viscothermal modeling model that has recently gained traction is the Boundary Layer Impedance (BLI) method [7,15–21]. The BLI is based on an impedance-like expression that is developed upon neglecting terms in a simplified version of the FLNS. As a consequence, the computational problem is reduced to similar complexity as the isentropic Helmholtz equation. However, using the BLI will in some cases come at the cost of reduced accuracy e.g. in narrow regions where the gap size is comparable to the viscous and thermal boundary layer width [16], or if the geometry has very large curvatures [17].

Shape optimization based on an underlying numerical method, such as the FEM or the BEM, is an engineering tool that potentially can aid the design process and create new innovative solutions to engineering problems. In the field of acoustics several examples exist of the utilization of shape optimization, e.g., optimization of acoustic horns [22–24], loudspeakers [25,26], compression driver phase plugs [26,27], noise barriers [28,29], hearing instruments [7], transient vibro-acoustics [30] and acoustic resonators including viscothermal losses [14]. Besides shape optimization, topology optimization has also become an important engineering design tool within the area of acoustics [31,32].

In this work, we investigate how the KD and the BLI models perform in the context of shape optimization. The models are evaluated by optimizing acoustic Helmholtz-like resonators using an axisymmetric boundary element formulation. Shape optimization, or optimization in general, is useful to explore the weaknesses of an underlying numerical model (BEM) since the optimizer will utilize any weakness, or error, in the numerical model. Therefore, using the BLI in an optimization context might create designs that are a product of a numerically inaccurate method rather than the underlying physics. Remark that employing a full shape optimization methodology for the design of Helmholtz-like resonators is overkill if the purpose of the presented work concerned the actual design of Helmholtz resonators. In that case, a simple sizing optimization using two to three parameters would be sufficient. However, as this work aims to illustrate potential pitfalls when including the BLI condition in a shape optimization approach, the Helmholtz resonators are chosen exactly due to their simplicity. That is, if the assumption of non-overlapping boundary layers is violated even for such a simple design problem, the issue is likely to be even more pronounced for more complicated design problems, and hence, design engineers should be made aware of this potential pitfall.

This work can be considered a natural extension of the results presented in a recent publication by the same authors in Andersen et al. 2019 [14]. Moreover, [14] adopts a simplified approach for the sensitivity analysis using finite difference, whereas this paper presents an improved semi-analytical discrete adjoint sensitivity analysis that can be applied to both the KD and the BLI implementations with better computational efficiency and accuracy.

The paper is organized as follows. First, the implementation of the KD and BLI into a BEM framework is discussed. This is followed by sections that describe the establishment and evaluation of two shape optimization test cases that will explore the validity of the BLI. Finally, the results of the test cases are used to discuss the benefits and the limitations of the BLI compared to the KD and the FLNS.

2. Boundary element method

Most of the work presented in this paper is based on the time-harmonic BEM formulation. The BEM takes its starting point at the Helmholtz-Kirchhoff integral equation given by

$$C(P)\,p(P) = \int_{\Gamma} \frac{\partial G(R)}{\partial n} p(Q)\,\mathrm{d}\Gamma - \int_{\Gamma} G(R)\,\frac{\partial p(Q)}{\partial n}\mathrm{d}\Gamma, \tag{1}$$

where C is the integral free term, P is the collocation point, Q is a position on the generator, $R = |P - Q|$, p is the unknown acoustic pressure, $G(R)$ is the Green's function in 3D and Γ represents the entire boundary. A positive time convention is adopted throughout the paper using $e^{j\omega t}$ where ω is the angular frequency. The studied examples are based on an axisymmetric assumption, therefore, Eq. (1) is written as

$$C(P)\,p(P) = \int_{L}\int_{0}^{2\pi} \frac{\partial G(R)}{\partial n} p(Q)\,\mathrm{d}\theta\mathrm{d}L - \int_{L}\int_{0}^{2\pi} G(R)\,\frac{\partial p(Q)}{\partial n}\mathrm{d}\theta\mathrm{d}L. \tag{2}$$

Discretization of Eq. (2) using direct collocation yields the system of equations

$$\mathbf{A}\mathbf{p} - \mathbf{B}\frac{\partial \mathbf{p}}{\partial n} = \mathbf{0}. \tag{3}$$

Here, the utilized implementation into axisymmetry is inspired by the work by P.M. Juhl [33]. The implementation uses a combination of elliptic integrals and recursive Gauss integration to handle the singular and near-singular integrals arising in the axisymmetric BEM formulation [34].

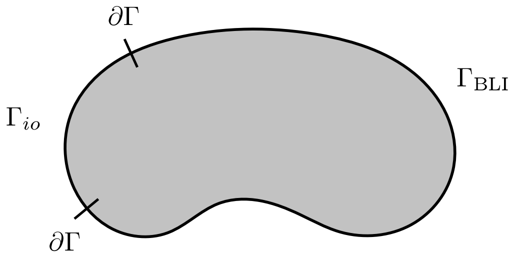

Fig. 1. A sketch of the boundary conditions used with the BLI-BEM. The gray area represents the interior acoustic domain.

3. Axisymmetric viscothermal BEM

Without any further simplifications, the FLNS can be reformulated into separate Helmholtz-like equations using the KD. The KD is given by [12,35,36]

$$\begin{aligned}
&\Delta p_a + k_a^2 p_a = 0, \\
&\Delta p_h + k_h^2 p_h = 0, \\
&\Delta \vec{v}_v + k_v^2 \vec{v}_v = \vec{0} \quad \text{with} \quad \nabla \cdot \vec{v}_v = 0,
\end{aligned} \tag{4}$$

where p_a, p_h, $\vec{v}_v$, k_a, k_h and k_v is the acoustic pressure, the thermal pressure, the viscous velocity, the acoustic wave number, the thermal wavenumber and the viscous wavenumber, respectively. Each of the equations in the KD can be modeled using BEM, i.e

$$\begin{aligned}
&\mathbf{A}_a \mathbf{p}_a - \mathbf{B}_a \frac{\partial \mathbf{p}_a}{\partial n} = \mathbf{0}, \\
&\mathbf{A}_h \mathbf{p}_h - \mathbf{B}_h \frac{\partial \mathbf{p}_h}{\partial n} = \mathbf{0}, \\
&\mathbf{A}_v \mathbf{v}_{v,r} - \mathbf{B}_v \frac{\partial \mathbf{v}_{v,r}}{\partial n} = \mathbf{0}, \\
&\mathbf{A}_v \mathbf{v}_{v,z} - \mathbf{B}_v \frac{\partial \mathbf{v}_{v,z}}{\partial n} = \mathbf{0},
\end{aligned} \tag{5}$$

where axisymmetry is assumed. Coupling of the discretized BEM equations require the fulfillment of the isothermal and no-slip boundary conditions, given by

$$\begin{aligned}
p &= \tau_a p_a + \tau_h p_h, \\
\vec{v}_b &= \phi_a \nabla p_a + \phi_h \nabla p_h + \vec{v}_v,
\end{aligned} \tag{6}$$

where τ_a, τ_h, ϕ_a and ϕ_h are constants that depend on frequency and viscothermal quantities. The boundary conditions can be applied following the approach in [37]. However, instead of solving the system of equations using a combination of Schur Complement operations or partially expanded system (see e.g. Refs. [13,14,37]), we will here establish a fully-coupled system avoiding the intermediate Schur operations. The system of equations becomes

$$\mathbf{S}_{\mathrm{KD}} \mathbf{x} = \mathbf{f}, \tag{7}$$

where $\mathbf{S}_{\mathrm{KD}}$ is the system matrix, $\mathbf{x}$ is the solution vector containing all the unknowns and $\mathbf{f}$ is a vector containing boundary velocity conditions. A more in-depth description of the assembly of the system can be found in Appendix A.

4. BEM using the boundary layer impedance method

Another interesting approach to include losses in the BEM is the BLI method. In the BLI, losses are approximated using an admittance condition [16,19], so the normal derivative of the pressure can be written as

$$\frac{\partial p}{\partial n} = \mathrm{i} k Y_{\mathrm{BLI}} p, \tag{8}$$

where the admittance Y_{BLI} is given by

$$Y_{\mathrm{BLI}} = \left[-\frac{\Delta_t}{k k_v} + (\gamma - 1)\frac{k}{k_h} \right], \tag{9}$$

where Δ_t is the tangential Laplacian and γ is the ratio of specific heats. Substitution of Eq. (8) into Eq. (1) and performing integration by parts yields

$$\begin{aligned}
C(P)\,p(P) = &\int_{\Gamma} \frac{\partial G(R)}{\partial n} p(Q)\,\mathrm{d}\Gamma - \int_{\Gamma_{io}} G(R) \frac{\partial p(Q)}{\partial n} \mathrm{d}\Gamma_{io} \\
&- \frac{\mathrm{i}}{k_v} \int_{\Gamma_{\mathrm{BLI}}} \nabla_t G(R) \cdot \nabla_t p(Q)\,\mathrm{d}\Gamma - (\gamma - 1)\frac{\mathrm{i}k^2}{k_h} \int_{\Gamma_{\mathrm{BLI}}} G(R)\,p(Q)\,\mathrm{d}\Gamma,
\end{aligned} \tag{10}$$

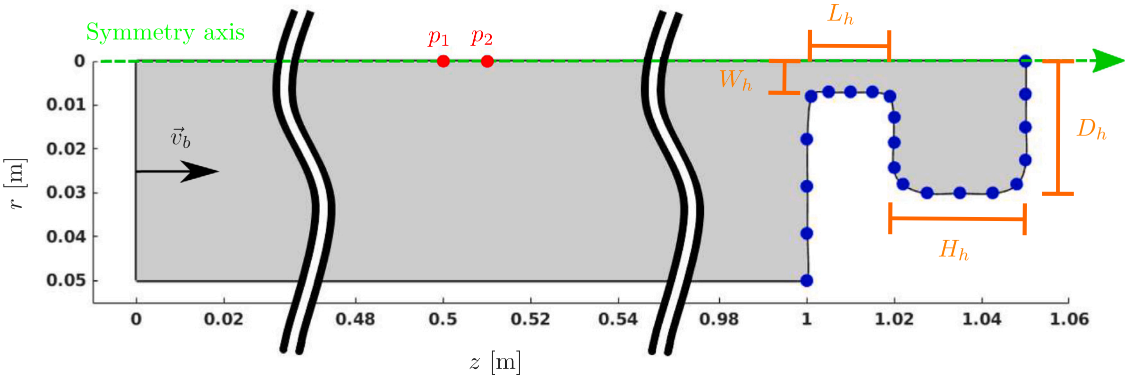

Fig. 2. Test case 1 - A Helmholtz resonator. (For interpretation of the references to color in this figure legend, the reader is referred to the web version of this article.)

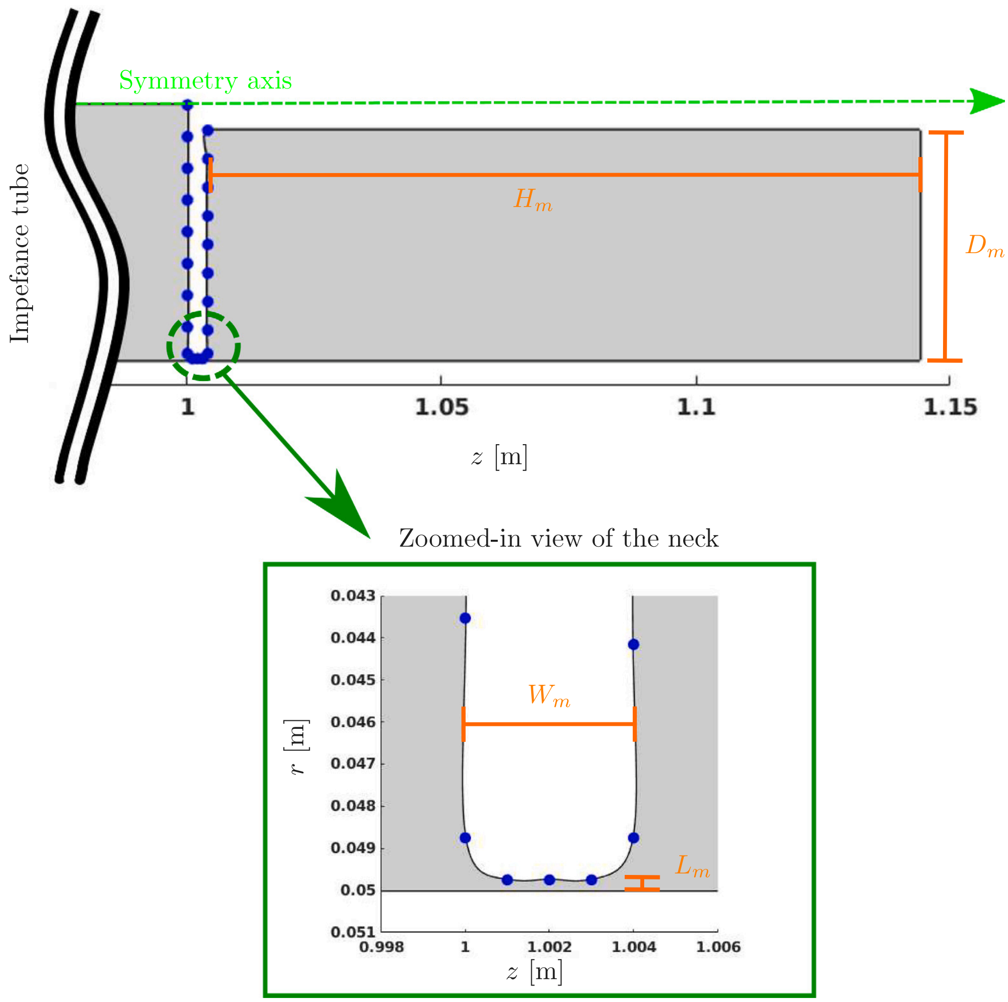

Fig. 3. Test case 2 - A micro-ring slit resonator.

where Γ_{io} represents the boundaries where $\frac{\partial p}{\partial n}$ is given in terms of a velocity condition and Γ_{BLI} is the boundaries where the BLI condition is applied. The entire boundary is $\Gamma = \Gamma_{io} \cup \Gamma_{\text{BLI}}$. A sketch of the definitions of the boundary conditions is shown in Fig. 1.

It should be noted that it is assumed that the tangential Laplacian can be modeled using [19]

$$\int_{\Gamma_{\mathrm{BLI}}} G(R)\,\Delta_t p\,\mathrm{d}\Gamma = -\int_{\Gamma_{\mathrm{BLI}}} \nabla_t G(R)\cdot\nabla_t p\,\mathrm{d}\Gamma \tag{11}$$

where the assumption is that [16]

$$\int_{\partial\Gamma_{\mathrm{BLI}}} G(R)\,\nabla_t p\cdot\mathbf{n}_t\,\mathrm{d}\partial\Gamma = 0, \tag{12}$$

where $\mathbf{n}_t$ is the unit-vector tangent to Γ_{BLI}. Eq. (10) is solved using the axisymmetric approach described in the Eqs. (2)–(3). The discretized system of equations is given in the compact form

$$\mathbf{S}_{\mathrm{BLI}}\mathbf{p} - \mathbf{B}_{io}\frac{\partial\mathbf{p}}{\partial n} = \mathbf{0}, \tag{13}$$

where the terms in Eq. (10), that depend on the pressure p, are contained within the matrix $\mathbf{S}_{\mathrm{BLI}}$. The matrix $\mathbf{B}_{io}$ is created from the second term on the right-hand-side of Eq. (10). Comparing Eq. (10) to the KD-BEM from Eq. (A.1), it is clear that the size of the BLI system is eight times smaller than its KD counterpart. This indicates a potential for significant computational savings which will be investigated further in the numerical example section.

5. Impedance tube test cases

Two shape optimization test cases are studied, which to a varying degree will challenge the KD and BLI implementations. Both of the test cases are based on an axisymmetric formulation of an impedance tube. However, the test cases deviate from each other by having a different initial geometry at the termination. The axisymmetric geometry of the entire impedance tube is depicted in Fig. 2. The computational problem is solved by imposing an arbitrary but realistic velocity condition $\vec{v}_b = 0.01$ m/s at one end of the tube. The opposite end of the tube is parameterized with an initial design of an acoustic resonator. In the first test case, the geometry is parameterized as a Helmholtz resonator. The size of the Helmholtz resonator is given by the parameters $W_h = 0.7$ cm, $L_h = 2$ cm, $H_n = 3$ cm and $D_n = 3$ cm. The parameters are shown in orange colors in Fig. 2 The second test case is an impedance tube with a Helmholtz-like resonator as shown in Fig. 3. However, here the neck is a very narrow circular ring slit located along the perimeter of the impedance tube cross section. The dimensions of the resonator are given in Fig. 3 by the parameters $W_m = 0.25$ mm, $L_m = 4$ mm, $H_m = 14$ cm and $D_m = 4.5$ cm. The first and second test cases are hereafter referred to as TC1 and TC2, respectively. It should be noted that the two different optimization test cases are limited in a way so that they cannot converge to the same design. The main objective of the resonator design problem is to make the resonators as absorbent as possible. In an impedance tube, the absorption coefficient can be obtained using the expression [38]

$$\phi = 1 - \left|\frac{\mathrm{e}^{-\mathrm{i}k_{\mathrm{LL}}d} - \frac{p_2}{p_1}}{\frac{p_2}{p_1} - \mathrm{e}^{\mathrm{i}k_{\mathrm{LL}}d}}\right|^2, \tag{14}$$

where ϕ is the absorption coefficient and k_{LL} is the lossless wavenumber. In Eq. (14), it is also necessary to evaluate the pressures p_1 and p_2 as defined in Fig. 2 where the distance $d = 1$ cm is chosen between their positions.

In Figs. 2 and 3, the geometry is parameterized so that the geometry can be changed by perturbing the control points, represented by the blue dots. The interpolation of the boundary mesh between the control points is mapped by the C^2 parabolic blending basis functions found in Ref. [39]. The control points will be used to alter the design during the optimization process. Large deformations of the parametrization can often lead to distorted meshes and thereby increase the numerical errors. This can be prevented using, e.g re-meshing during the optimization. However, in the test cases presented here, the initial mesh is discretized with a very fine mesh in the parameterized region, making re-meshing unnecessary.

6. Optimization problem

The optimization problem is to maximize the absorption of the two resonators defined in TC1 and TC2. The goal is to observe the differences in performance and optimized geometries when the optimization is carried out with either the KD-BEM or BLI-formulation. Formally the optimization problem is stated as,

$$\begin{aligned}
\max_{\rho}:\quad & \phi(\mathbf{x}(\rho),\rho)\\
\text{s.t.}\quad & \left(\frac{1}{N_n}\sum_{j=1}^{N_n}\kappa_j(\rho)^{\sigma}\right)^{1/\sigma} - \kappa_{max} \le 0,\\
& D_{min} - \beta\frac{1}{N_c}\sum_{j=1}^{N_c} D_j(\rho) \le 0,\\
& \text{Governingequation},\\
& 0 \le \rho_i \le 1,
\end{aligned} \tag{15}$$

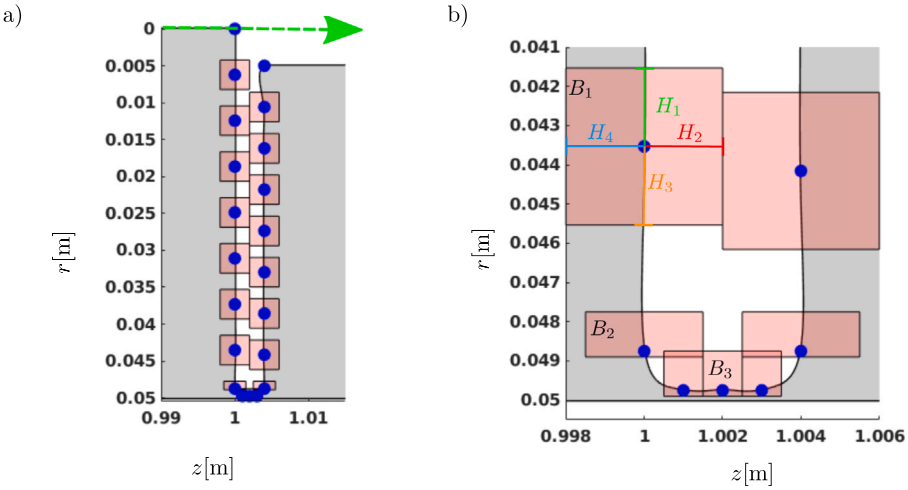

Fig. 4. Test case 2 - the box constraints used to limit the movement of the control points. The bounds in witch the control points can move are given by the red areas. In the figure, (a) are the bounds for all the control points and (b) is a zoom-in picture of the bounds in the ring slit. The dimensions of three different box constraint types (B_1, B_2 and B_3) are given in Table 1.

Table 1
The size of the three different box constraints used in TC2.

	H_1 [mm]	H_2 [mm]	H_3 [mm]	H_4 [mm]
B_1	2	2	2	2
B_2	1	1.5	0.15	1.5
B_3	1	0.5	0.15	0.5

where $\phi(\mathbf{x}(\rho), \rho)$ is the objective function depending on the state vector $\mathbf{x}(\rho)$ and the design variable vector ρ with ρ_i being the ith entry in ρ. The design variables are defined in terms of the rz-coordinates of the control points. Moreover, the problem is constrained with non-linear constraints to avoid non-physical behavior. In the definition of the non-linear constraints, κ_j is the curvature of the boundary at discrete computational nodes, N_n is the number of nodes in the mesh, κ_{max} is the maximum allowed curvature, $\sigma = 15$ is exponent in the generalized mean, D_j is the distance between control points, N_c is the number of control points, D_{min} is the minimum allowed distance between control points and β is a boundary overlap detection variable that is either -1 or 1 when no overlap or an overlap is present, respectively. The non-linear constraints and their evaluation are the same as in Ref. [14]. However, it should be noted that the curvature constraints and distance constraints are in this case evaluated as a generalized mean and average values lead to only two constrains. This is different from Ref. [14] where constraints are defined for individual nodes and control points, resulting in hundreds of constraints. TC1 and TC2 use the same limit on the allowed curvature with $\kappa_{max} = 1250\ \mathrm{m}^{-1}$. The minimum distance D_{min} is set to 2 cm in TC1 and 1.8 cm in TC2. As it might be observed, these values of D_{min} are larger than the actual minimum distance in the two initial designs. However, due to the averaging of the individual distances D_j, the value of D_{min} needs to be chosen slightly larger, if the initial design is to fulfill the constraint. The same is the case for the curvature constraint. The movement of the control points is limited by a set of scaled box constraints, so that

$$\rho_i = \frac{u_i - L_{l,i}}{L_{h,i} - L_{l,i}}. \tag{16}$$

Hereby, ρ_i is scaled so $0 \leq \rho_i \leq 1$. Furthermore, u_i is a Cartesian r or z-coordinate of a control point. The movement of a control point is limited by its upper and lower bounds $L_{l,i}$ and $L_{h,i}$, respectively. The upper and lower bounds are different between the two test cases but also different among the individual control points. In TC1 the control points can move ±1.5 cm from their initial position except control points close to the symmetry axis which are limited to never cross the axis of symmetry, i.e, there is always a minimum of 2 mm between the control point and the symmetry axis. Additionally, the control point lying on the symmetry axis can only move in the r-direction and the control point connecting the design domain to the impedance tube is not allowed to move at all. In TC2 the bounds are more complicated as compared to TC1, as depicted in Fig. 4. It should be noted that the box constraints in the slit are made so that the parametric boundaries cannot overlap the opposing side of the slit. The bounds used in the optimization of TC2 consist of three different magnitudes represented by B_1, B_2 and B_3 in Fig. 4b. Also in the figure, the variables H_1, H_2, H_3 and H_4 represent the distance the control point can move in the rz-direction from its initial position. The sizes for the three different types of bounds are given in Table 1.

The optimization algorithm used to solve Eq. (15) is the sequential quadratic programming implementation in the MATLAB function "fmincon".

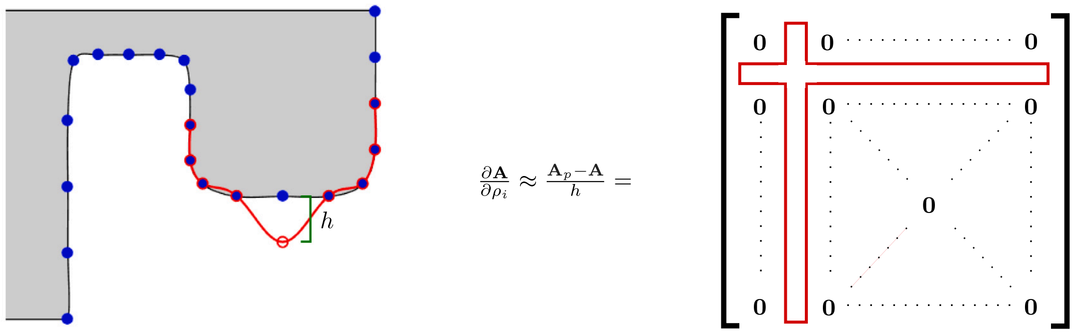

Fig. 5. Reduced assembly of matrix derivatives. On the left-hand side, the parameterized Helmholtz resonator is presented with the blue dots being the control points. The red line with circles represents the geometry that is affected when perturbing a single design variable with a step length h. Depicted on the right-hand side is the resulting BEM matrix showing how only some of the rows and columns (marked with red) will be affected due to the change in ρ_i. The matrix $\mathbf{A}_p$ is the matrix created from the perturbed geometry. (For interpretation of the references to color in this figure legend, the reader is referred to the web version of this article.)

7. Semi-analytical adjoint sensitivities

An efficient and fast evaluation of the gradients, or sensitivity information, is an important factor for making the shape optimization approach capable of handling a large set of design variables. A common approach for isentropic acoustic BEM is to develop the sensitivities using the continuous equations applying e.g. direct differentiation [29,40] or an adjoint method [41,42]. In the following, we present how gradients can be obtained using a discrete semi-analytical adjoint approach. The adjoint equation for time-harmonic acoustic problems can be written following [31,43] as

$$\mathbf{S}^{\mathrm{T}}\lambda = -\left(\frac{\partial \phi_0}{\partial \mathbf{x}_r} - \mathrm{i}\frac{\partial \phi_0}{\partial \mathbf{x}_i}\right)^{\mathrm{T}}, \tag{17}$$

where λ is a vector with the Lagrange multipliers and the subscripts r and i denote the real and imaginary part of the state variables, respectively. The system matrix $\mathbf{S}$ can either be $\mathbf{S}_{\mathrm{KD}}$ or $\mathbf{S}_{\mathrm{BLI}}$. Hereafter, the sensitivities can be found by solving the sensitivity problem

$$\frac{\mathrm{d}\phi}{\mathrm{d}\rho_i} = \frac{\partial \phi_0}{\partial \rho_i} + \Re\left(\lambda^{\mathrm{T}}\left(\frac{\partial \mathbf{S}}{\partial \rho_i}\mathbf{x} - \frac{\partial \mathbf{f}}{\partial \rho_i}\right)\right), \tag{18}$$

where ρ_i is a single design variable. An in-depth description of the evaluation of the right-hand side in Eq. (17) and the term $\frac{\partial \phi_0}{\partial \rho_i}$ in Eq. (18) is given in Appendix B. The approach can be applied to both the KD and BLI formulations. However, making it efficient for BEM problems requires further development and care when performing the assembly of the matrix derivatives. In this work, it is proposed to use a reduced assembly approach to circumvent the possible inefficiency issue arising if the matrix derivatives are evaluated for all the entries in the dense matrix.

7.1. Reduced assembly

For small to medium-sized BEM problems, the assembly of the coefficient matrices is the most computationally demanding part. Therefore, performing the assembly of $\frac{\partial \mathbf{S}}{\partial \rho_i}$ poses a potentially large reduction in the computational efficiency of the semi-analytical approach. To circumvent this potential issue, it is proposed to carry out the matrix derivatives using a reduced assembly approach where only non-zero entries in the derivative matrix are assembled. The approach is sketched in Fig. 5. A similar semi-analytical reduced assembly approach for isentropic acoustic BEM can be found in [14]. The reduced assembly approach is here extended to also work for the $\mathbf{S}_{\mathrm{KD}}$ and $\mathbf{S}_{\mathrm{BLI}}$ matrices. The finite difference evaluation of the matrix is performed so a perturbed design variable is given by

$$\rho_p = \rho_i + h \tag{19}$$

where ρ_p is the perturbed design variable, ρ_i is the initial design variable and h is the step length of the perturbation. The step length used to create the matrix derivatives is $h = 10^{-6}$. The step length was chosen by sweeping different step lengths between 10^{-16} and 10^{-1} and using a step length in a region where the sensitivities vary very little with respect to step length. A similar approach is discussed in Ref [14] and Appendix B. It should be noted that for the reduced assembly to be efficient it is required that the design variables and parametrization have compact support.

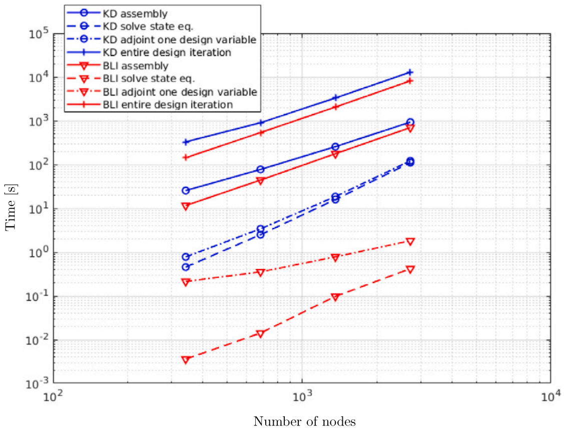

Fig. 6. Comparison of the computational efficiency between the KD-BEM and the BLI-BEM. The computations are based on the geometry and the parametrization in TC1.

8. Numerical investigations

In this section, the differences between the KD-BEM and the BLI-BEM in terms of efficiency and accuracy in a shape optimization setting are investigated. Selected studies also include full FEM FLNS and BLI simulations for comparison. The results are presented as follows. First, an efficiency study is carried out with a focus on the computational speed of the system assembly, the solution of the state equation, and the semi-analytical sensitivity analysis. Hereafter, the shape optimization results of the two test cases TC1 and TC2 are presented. The shape optimization in TC1 is performed assuming an excitation frequency of 250 Hz, whereas TC2 contains optimization results ranging from 200 Hz to 275 Hz. The optimization frequencies are chosen since they are close to the resonance frequencies of the initial geometries and will in TC2 create boundary layers in the limit of overlap or completely overlapping. When the KD-BEM and the BLI-BEM are compared, the underlying computational mesh will remain the same. All simulation and optimization results in the paper are performed using a workstation with a Xeon E5-1650 v3 CPU and 128 GB RAM.

8.1. *Efficiency comparison of the KD-BEM and the BLI-BEM*

The main goal behind the BLI method is to reduce the computational complexity required to solve a viscothermal acoustic problem. In this work, both viscothermal BEM implementations are based on a MATLAB MEX/C++ environment where the assembly of the matrix entries is carried out in compiled C++ code with the addition of OpenMP parallelization. Moreover, the KD-BEM is a speed-optimized code using the truncation approach in [14] to improve the assembly speed of the viscous and thermal matrices by avoiding the assembly of noncontributing zero-valued entries. To give an idea of the efficiency benefits when using the BLI-BEM as compared to KD-BEM, speed measures of the assembly of the system matrices, solving the state equations, and the sensitivity analysis are given in Fig. 6. Timings of the code are based on the "tic-toc" stopwatch in MATLAB. In the figure, the solution to Eqs. (7), (13) and (18) is done using the MATLAB function "mldivide". From Fig. 6 it is evident that the BLI-BEM has major benefits in terms of the solution time and the speed of the sensitivity analysis. Interestingly, due to the truncation approach the assembly time of $\mathbf{S}_{\mathrm{KD}}$ is only slightly higher that of $\mathbf{S}_{\mathrm{BLI}}$, even though it requires the additional assembly of $\mathbf{A}_h$, $\mathbf{A}_v$, $\mathbf{B}_h$ and $\mathbf{B}_v$. Furthermore, because the assembly speed of $\mathbf{S}_{\mathrm{KD}}$ is mainly dominated by $\mathbf{A}_a$ and $\mathbf{B}_a$ the scaling for higher mesh densities is close to being the same to the assembly of $\mathbf{S}_{\mathrm{BLI}}$. For the coarsest mesh the total BLI speed-up for an entire design iteration including all design variables in TC1 is 2.3 whereas it is 1.6 for the finest mesh. While the speed-up of BLI-BEM is approximately twice that of KD-BEM, the memory requirement for storing the system matrices scales very different between the KD-BEM and the BLI-BEM. For the coarsest mesh the memory footprint of $\mathbf{S}_{\mathrm{KD}}$ is 115 MB and 1.8 MB for $\mathbf{S}_{\mathrm{BLI}}$. The finest mesh requires 11 GB and 112 MB to store $\mathbf{S}_{\mathrm{KD}}$ and $\mathbf{S}_{\mathrm{BLI}}$, respectively. It should be noted that $\mathbf{S}_{\mathrm{KD}}$ in theory only contains dense regions where $\mathbf{A}_a$ and $\mathbf{B}_a$ are stored. This sparsity can be leveraged by using a different format to store the system matrix, maybe used in combination with an iterative solver. If this is done, the storage requirements will be only slightly larger than that of isentropic BEM. Nevertheless, in the presented work $\mathbf{S}_{\mathrm{KD}}$ is stored as a fully populated matrix.

8.2. *TC1 - optimization of a Helmholtz resonator*

For TC1 the optimization is performed using both the KD-BEM and the BLI-BEM as the underlying models. The optimized designs for the two cases are displayed in Figs. 7 and 8. In Fig. 7a, the revolved design is displayed with the internal field variable being the sound pressure level (SPL). As expected, a high sound pressure is observed inside the cavity of the resonator, which is the way a Helmholtz resonator would operate close to its resonance. To show the behavior of the viscothermal quantities, the logarithm of the magnitudes of the field variables p_h and $\vec{v}_v$ are also plotted in Fig. 7b and c, respectively. Corresponding optimization plots

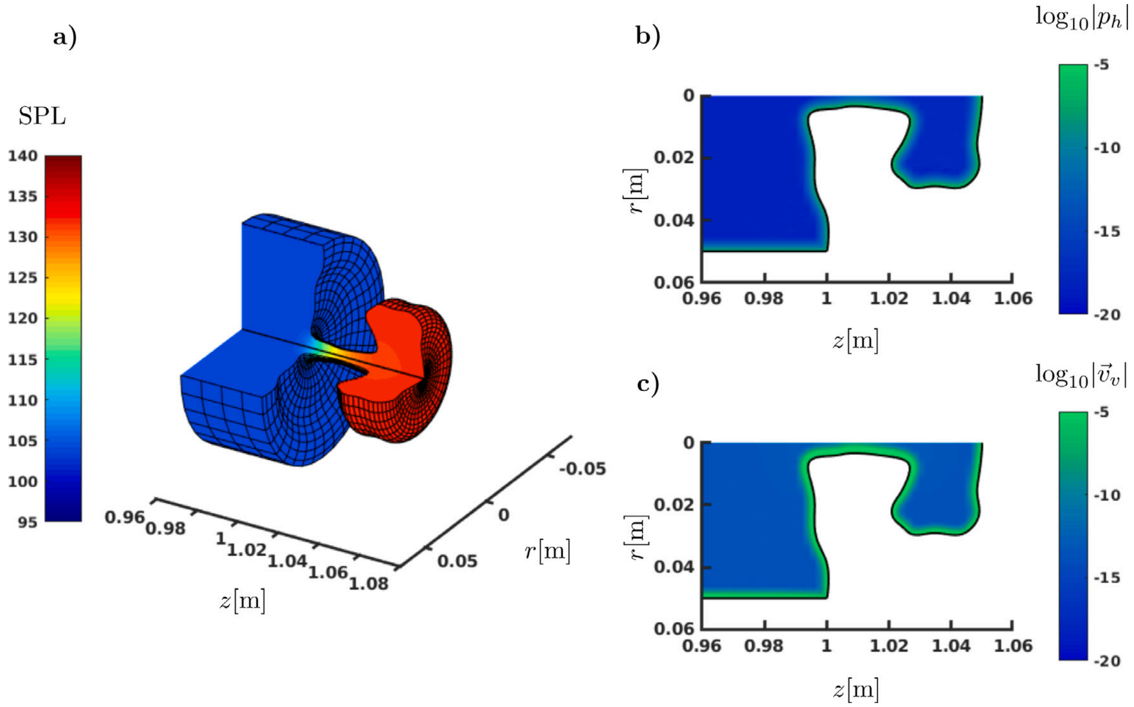

Fig. 7. The shape optimized design of the Helmholtz resonator optimized using the KD-BEM implementation. In the figure, (a) is the revolved design showing the sound pressure level, (b) is the thermal pressure p_h for the optimized design and similarly (c) plots the magnitude of viscous velocity $\vec{v}_v$. The field variable simulation is performed at the optimization frequency of 250 Hz.

using the BLI-BEM during the optimization are likewise plotted in the Figs. 8a, b and c. It should be noted that even though the optimization is based on the BLI-BEM, the field variables in the three plots are calculated with the KD-BEM to obtain the plots of the viscous and thermal quantities. Studying the differences in the field variables, it can be observed that the SPL is slightly higher inside the cavity of the design in Fig. 7a. However, the plots of p_h and $\vec{v}_v$ are similar for the two optimization cases.

When comparing the two optimized designs, the neck and cavity seem to converge toward slightly different design choices. It is expected that the influence of losses is most relevant in the neck. The neck in the KD-BEM-based design has its narrowest point at the center of the neck. Conversely, the design using BLI-BEM is more narrow at the entrance to the neck and the neck-cavity connection. Furthermore, the shapes of the optimized cavities are also different.

To further compare the KD and the BLI based designs, the frequency responses of the objective function for the two optimization cases are plotted in Fig. 9a and b, respectively. The figures contain simulations using both the KD-BEM and the BLI-BEM to evaluate the two designs. It is seen that the designs yield very similar absorption performance. As is evident, the two viscothermal implementations also give the same absorption responses near the optimization frequency. Additionally, both of the designs show near-perfect absorption at 250 Hz optimization frequency. However, perfect absorption for single frequency optimization of resonators has proven easy to obtain [14]. Only very small deviations between the two methods in the absorption response are observed below 220 Hz and above 280 Hz. The exact origin of the deviations is not investigated further, but they might be related to different mesh resolution requirement between the two viscothermal models.

8.3. TC2 - optimization of a micro ring slit resonator

As opposed to TC1, TC2 is meant as a test case that is performing optimization on the limits of what the BLI method accurately can model, i.e. the initial design guesses contain close to overlapping boundaries or completely overlapping boundaries. The results for the initial design, and the optimized results with KD-BEM and BLI-BEM are plotted in Fig. 10. The dashed red lines in the figure indicate the theoretical viscous boundary layer thickness calculated with the expression in [36, pp. 286]. In the figure, it is observed that the design optimized with BLI-BEM creates a deep overlap of the boundary layers whereas the optimization design obtained using KD-BEM only has very little overlap.

Additionally, the SPL results for the designs optimized with KD-BEM and BLI-BEM are plotted in Fig. 11a and b, respectively. In both figures, the SPL is obtained by the KD-BEM, which is expected to be more accurate in the given scenario. From the figures, it is observed that the design based on the BLI has a much lower internal SPL in the back-cavity. This is a first indication that the BLI method is challenged by the geometry at hand even though the boundary overlap makes up for very little of the overall computational domain.

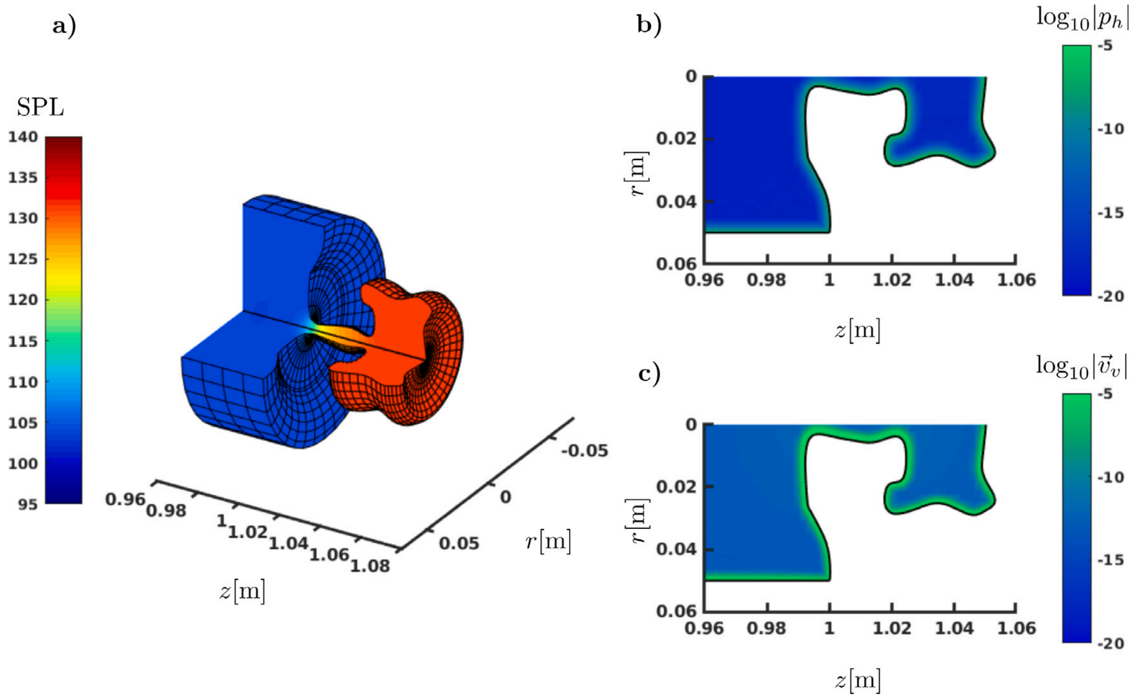

Fig. 8. The shape optimized design of the Helmholtz resonator optimized using the BLI-BEM implementation. The field variables are however calculated with the KD-BEM as BLI-BEM cannot calculate boundary layer regions. In the figure, (a) is the revolved design showing the SPL, (b) is the thermal pressure p_h for the optimized design and similarly (c) plots the magnitude of viscous velocity $\vec{v}_v$. The field variable simulation is performed at the optimization frequency of 250 Hz.

To further show the inaccurate behavior or non-optimal design created by the BLI-BEM-based optimization, the objective function as a function of frequency is plotted for the two designs in 12a and b. Fig. 12a shows how the design based on the KD-BEM has near-perfect absorption at 250 Hz. However, this is not the case if evaluated with BLI-BEM where the absorption coefficient is close to 95%. For all frequencies below the operating frequencies, the BLI-BEM underestimates the actual absorption coefficient. This is also in line with the acoustic boundary theory. The acoustic boundary thickness will increase for lower frequencies and thereby making the overlap of boundaries even larger for a constant geometry which poses a challenge for the BLI approach as it cannot handle overlaps. If the BLI-BEM is used in the optimization process, as in Fig. 12b, the design might appear to be working with near-perfect absorption at the optimization frequency. However, if the same design is computed with KD-BEM the design only yields 80% absorption.

In both Fig. 12a and b, the designs and the two BEM implementations are also validated with corresponding FEM FLNS (dashed green line) and BLI (dashed black line) simulations. The FEM simulations are performed in COMSOL Multiphysics using the "Thermoviscous" module and equation-based modeling to implement the BLI. It should be noted, that equation-based modeling is used because this work was developed before the BLI became a standard feature in the COMSOL "Acoustic" module. Interestingly, the KD-based design in Fig. 12a has a much broader frequency range with high absorption as compared to the resonator designs obtained in TC1. However, this can be attributed to the fact that the cavity volume in TC2 is more than three times that of TC1 [44, pp. 217]. The amplitude of the z-component of the viscous velocity is plotted in Fig. 13 for the two design optimizations. As is seen, the z-component becomes large in the proximity of where the boundary layers are overlapping. It is expected, and observed, that the optimized design with KD-BEM (Fig. 13a) creates only a small amount of boundary layer overlap so that the slit is not too resistive and acoustic energy can still propagate into the resonator cavity. The balance between slit resistivity and ease of propagation requires that opposing boundaries can "feel" each other's contribution to the boundary layer behavior. The BLI cannot capture this interaction between the boundary layers and creates complete boundary overlap.

8.4. TC2 - dependency on the initial design

The outcome of shape optimization is typically very dependent on the initial starting guess. Therefore, two additional optimization cases with different starting guesses are performed on TC2. In Fig. 14, the two optimization cases are shown. The starting guesses consist of two examples: no overlap and complete overlap of the theoretical boundary layer. The figure includes zoomed-in pictures of the geometry at the ring slit for the initial and the four shape optimized designs. Looking at the optimization results, it is seen that the design based on the KD continues to only have slightly overlapping boundary layers. On the contrary, the design based on the BLI prefers to have boundary layers that are completely overlapping in the slit. Similar to previous results in

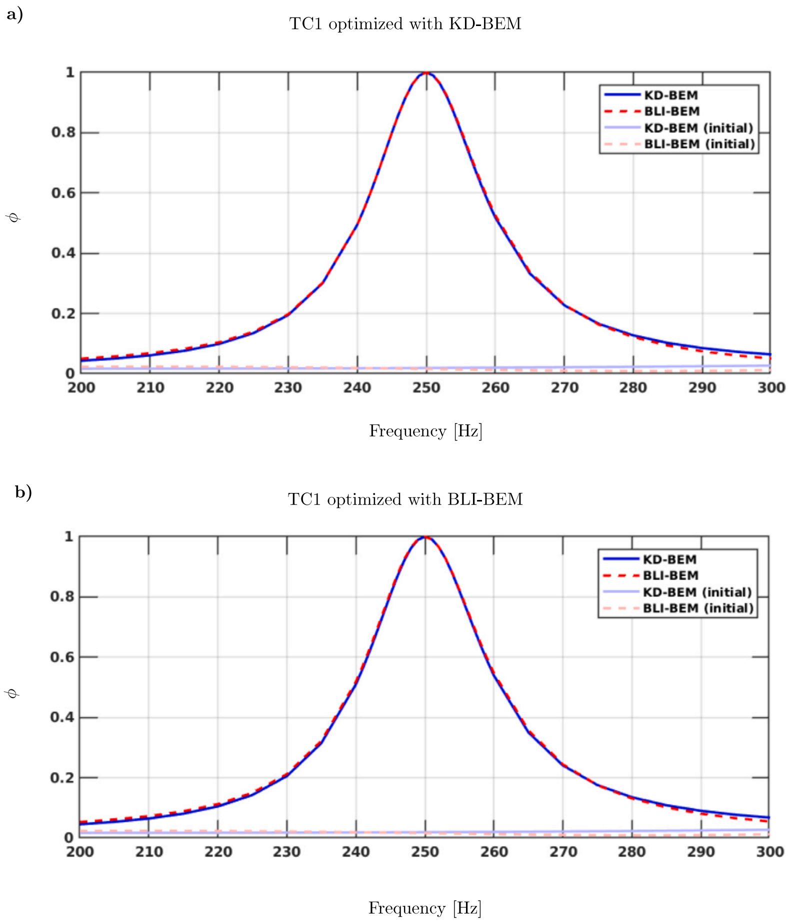

Fig. 9. The absorption coefficient frequency response of the two optimized resonator designs obtained in TC1. Both designs are evaluated using both the KD-BEM and the BLI-BEM. Figure (a) is the design optimized using the KD and Figure (b) is the design optimized using the BLI to account for the losses. Both figures also include the absorption curves for the initial design.

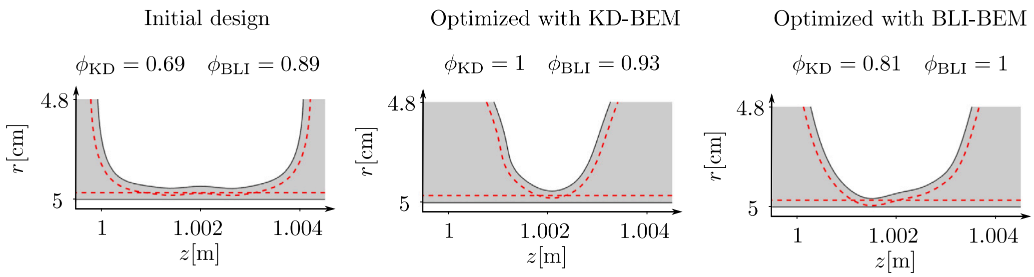

Fig. 10. Zoomed-in view of the resonator ring slit used in TC2. The plot includes the initial design, the design optimized with KD-BEM and the design optimized with BLI-BEM. Red-dashed lines represent the theoretical viscous boundary thickness at the optimization frequency (250 Hz).

Fig. 10, the designs that are optimized with BLI apparently yield 100% absorption. However, when the designs are cross evaluated with KD-BEM, their absorption coefficients are less that 92%.

8.5. TC2 - dependency on optimization frequency

The frequency at which the optimization is performed will also have an effect on the design of the resonator. The optimization test cases so far have been carried out at 250 Hz. Lowering the optimization frequency will yield a larger boundary layer thickness,

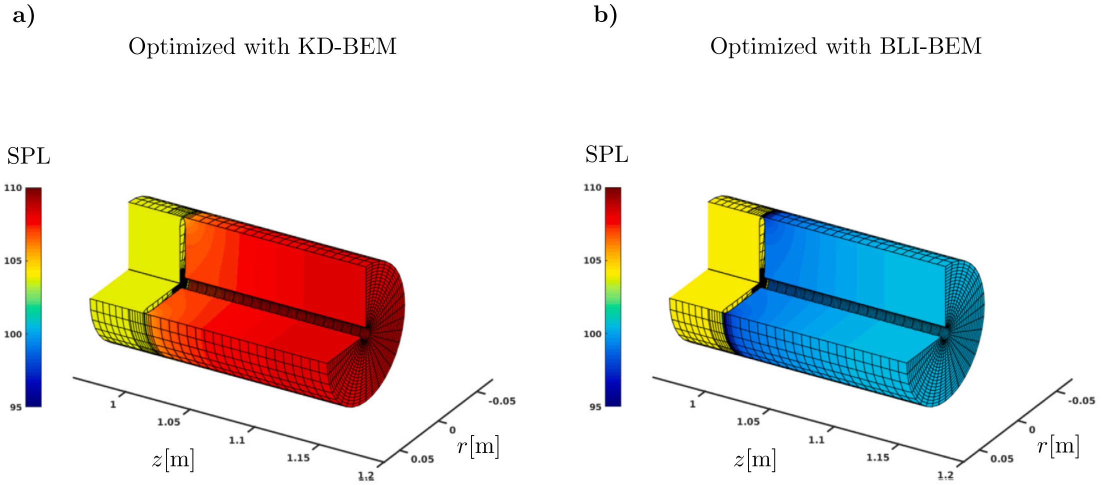

Fig. 11. The sound pressure level inside the two optimized designs in TC2. In the figure, (a) is the design optimized with KD-BEM and (b) is the design optimized with BLI-BEM. The field variables are in both plots obtained using the KD-BEM implementation.

hence, it might be logical to think that this will create more problems for the BLI method, i.e. boundary layer overlap. However, when the optimization frequency is lowered the length of the ring slit is increased and no overlap of the boundary layers is necessary in order to create a resonator with perfect absorption. This effect is seen in Fig. 15 where optimization is performed at 200, 225 and 275 Hz. On the other hand, optimization at 275 Hz results in a very short neck and boundary layers that are close to overlapping. It should be noted that the KD-BEM optimization at 275 Hz only results in close to perfect absorption. This is attributed to the optimization problem becoming more difficult, i.e., requiring a large curvature to create a very short neck. On the other hand, the BLI-BEM design at 275 Hz contains boundary layer overlap and as a result has a poorer performance as compared to the design optimized with KD-BEM.

9. Conclusions

The computational efficiency of the BLI compared to KD in the optimization cases shown in the presented work is evident, especially in an optimization context where more efficient methods are always sought. In the presented work, a design iteration using BLI-BEM is approximately twice as fast as compared to optimization using KD-BEM. The computational efficiency will presumably be even be greater for large 3D problems where the vector formulation of the KD-BEM will include additional degrees of freedom for the viscous velocity. It should be noted that the focus here has been on the BLI applied into a BEM implementation where small to medium sized problems are dominated by the assembly of the system matrix. The computational speed benefits of using the BLI as compared to the FLNS in a finite element context are much greater [16].

From our observations, BLI-BEM can comfortably be used if the parametrization by default will never yield boundary layer overlap in the frequency range of interest. However, if there exists any chance of overlap during the optimization it should be avoided: just some overlap can potentially lead to optimization of the numerical error, poorer performing designs, or even wrong results. Therefore, if some boundary overlap is detected during optimization it is highly recommended that the design is validated with a full method using the FLNS or the KD. Boundary Layer detection could also be implemented as a non-linear constraint using e.g the distance constraint. However, such constraint would complicate the optimization process and potentially make convergence to a stationary point more difficult, i.e, leading to poorer performing designs. Large geometric curvatures can also potentially lead to inaccuracies when using the BLI implementation [17]. However, this does not seem to have been provoked in the presented shape optimization results where the geometry have been bound by a curvature constraint.

Additionally, the presented work has shown how the well-known discrete adjoint approach can be used to obtain the shape sensitivities of both the KD-BEM and BLI-BEM implementations. To make this approach efficient, it is important to use a parametrization with compact support for which we have proposed a reduced assembly approach.

As a byproduct, TC2 has shown how using a combination of a narrow ring slits in the resonator design and a larger cavity can greatly improve the bandwidth of the absorption response. This could be useful in the design of meta-structure absorbers where most of the literature seems to use standard Helmholtz resonators similar to TC1 [45–47]. These results can only be obtained using optimization with a full linearized viscothermal model. It should be noted, that narrow slits and holes are commonly used in acoustic micro-perforated plate absorbers [11,48].

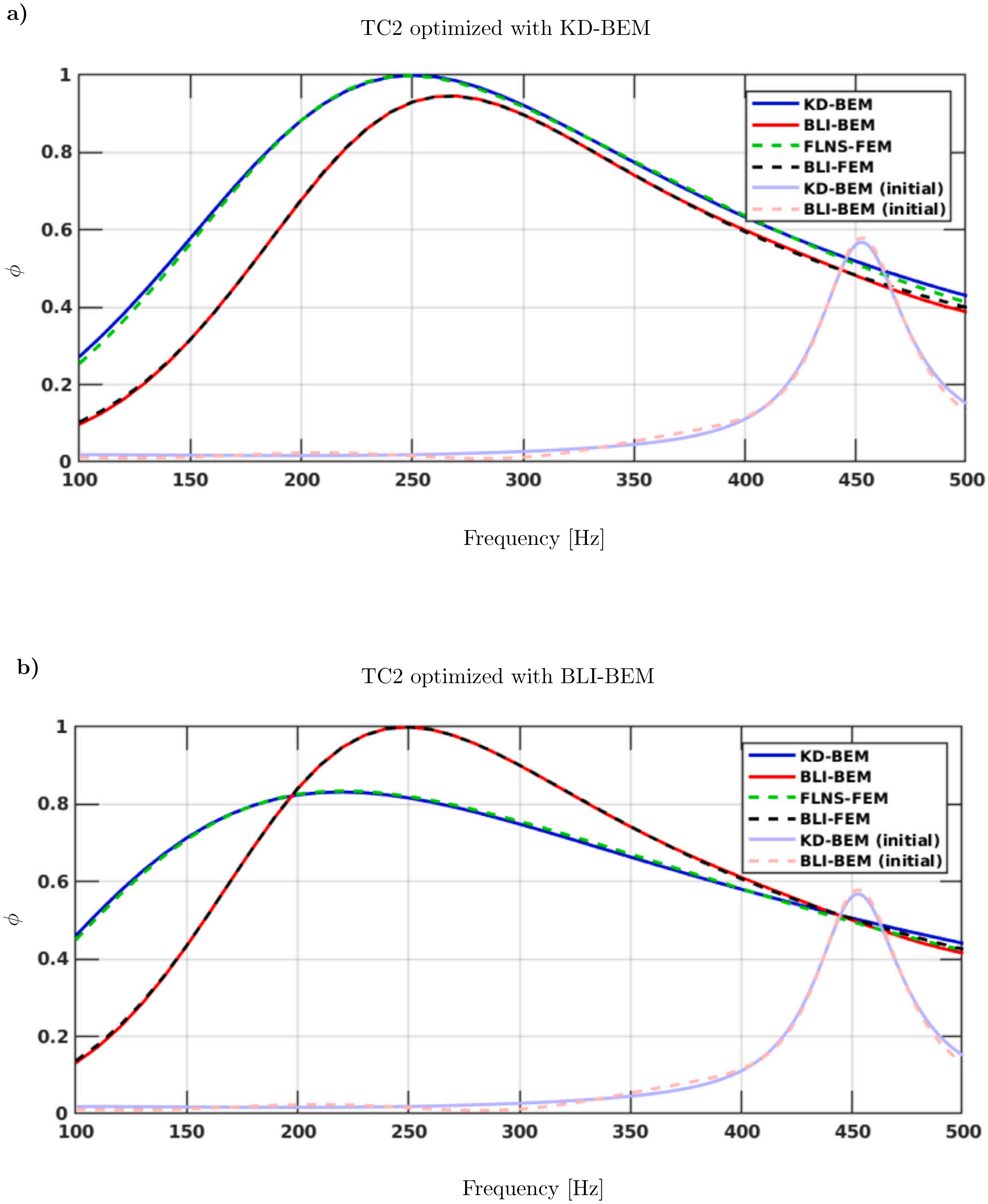

Fig. 12. The absorption coefficient as a function of frequency obtained from TC2. In the figure, (a) is the design optimized with KD-BEM and (b) is the design optimized with BLI-BEM. The absorption coefficients for the two design cases are also validated with FEM FLNS simulations and BLI FEM simulations. The FEM calculations are performed in COMSOL Multiphysics. Both figures also include the absorption curves for the initial design. (For interpretation of the references to color in this figure legend, the reader is referred to the web version of this article.)

While the FLNS and the KD viscothermal models are used as an accurate representation of the viscothermal losses, non-linear effects, such as vortex shedding in the ring slit, might be very relevant to include [49,50]. Therefore, it might also be necessary to perform non-linear time-domain Navier Stokes validation simulations of the optimized designs or perform measurements of the designs to validate the use of the linearized Navier Stokes. However, this is considered beyond the scope of this paper.

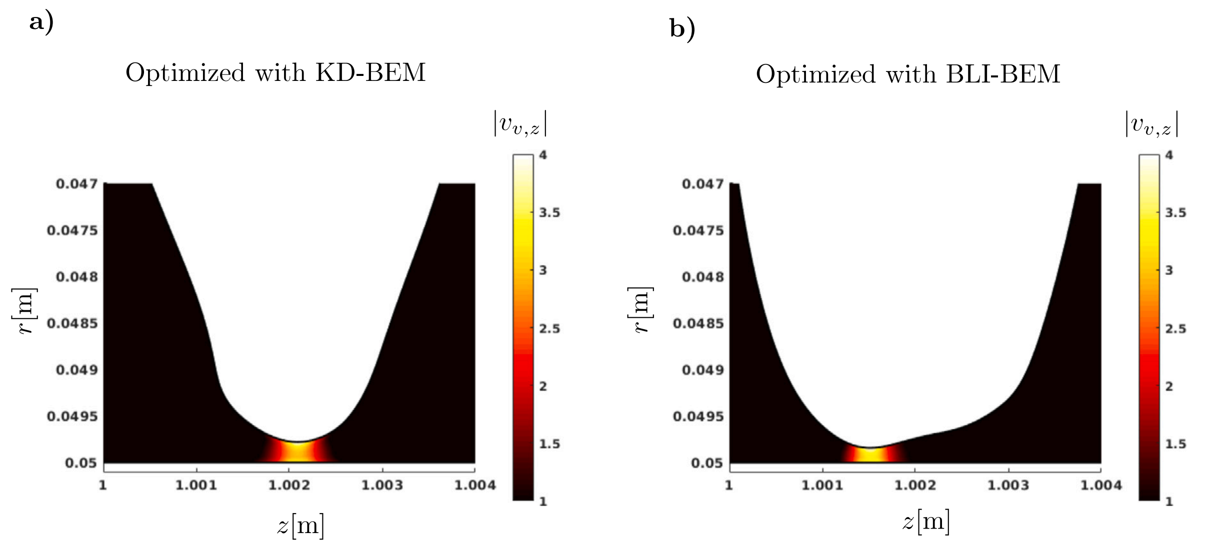

Fig. 13. The amplitude of the z-component of the viscous velocity for TC2. In the figure, (a) is the design optimized with KD-BEM and (b) is the design optimized BLI-BEM.

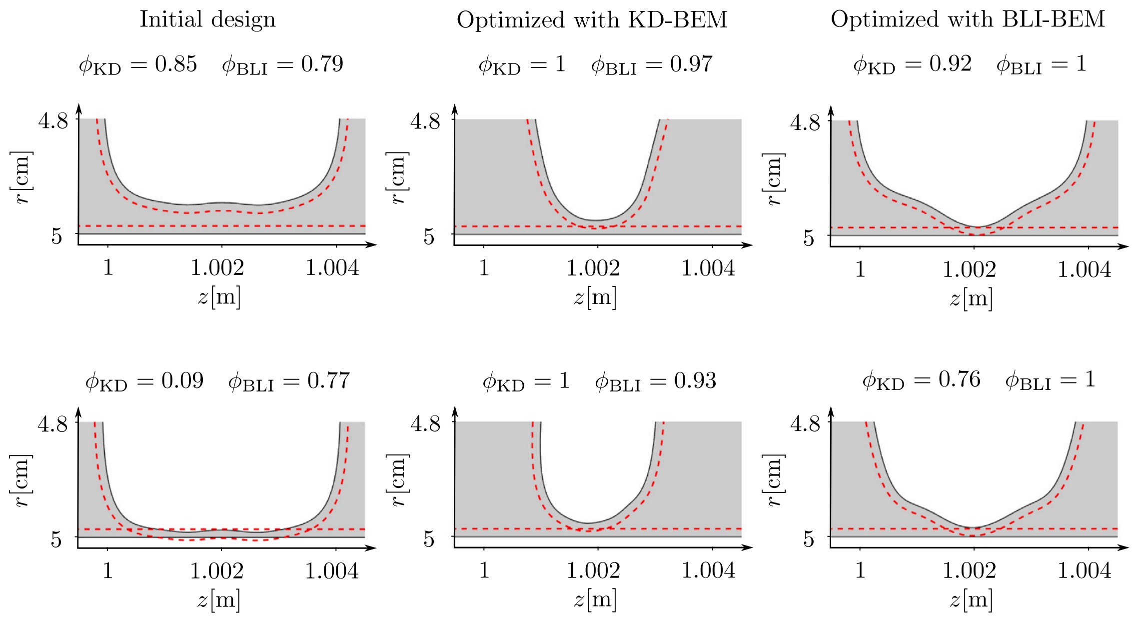

Fig. 14. Zoomed-in view of the resonator ring slit used in TC2. The plot includes the initial design, the design optimized with KD-BEM and the design optimized with BLI-BEM. Red-dashed lines represent the theoretical viscous boundary thickness at the optimization frequency (250 Hz).

In summary, the BLI is an attractive method to model viscous and thermal dissipation and its efficiency also makes it a good candidate for performing shape optimization. However, if it is used in an optimization context where the design space allows for boundary layer overlap, the BLI can potentially optimize for the inaccuracies of the numerical model rather than the true viscothermal effects. Therefore, a seemingly good design optimized with BLI can be sub-optimal in terms of the true performance. This is evident in TC2 where in some cases, including the full viscothermal effects is required to obtain a properly optimized design.

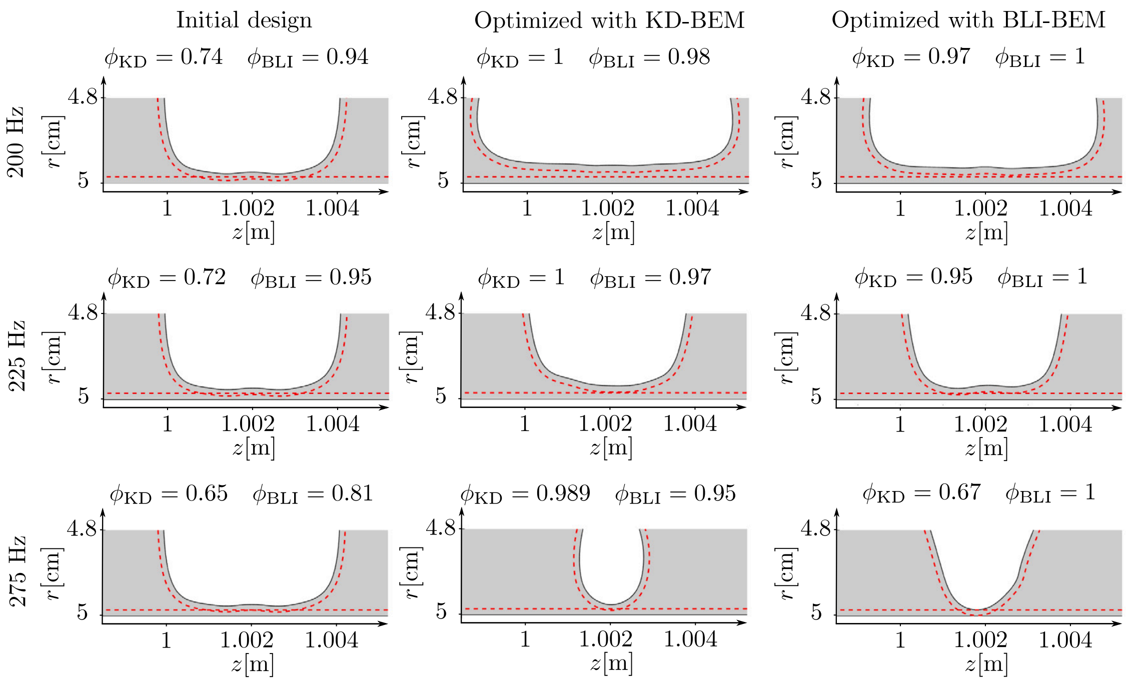

Fig. 15. Zoomed-in view of the resonator ring slit used in TC2. The plot includes the initial design, the design optimized with KD-BEM and the design optimized with BLI-BEM. Red-dashed lines represent the theoretical viscous boundary thickness. The three optimization cases are using the same initial design. The optimization frequencies are 200, 225 and 275 Hz, respectively.

CRediT authorship contribution statement

Peter Risby Andersen: Writing – original draft, Conceptualization, Methodology, Software, Investigation, Visualization. **Vicente Cutanda Henríquez:** Writing – review & editing, Conceptualization, Methodology. **Niels Aage:** Writing – review & editing, Conceptualization, Methodology.

Declaration of competing interest

The authors declare that they have no known competing financial interests or personal relationships that could have appeared to influence the work reported in this paper.

Data availability

The authors are unable or have chosen not to specify which data has been used.

Appendix A. Fully coupled system of equations for KD-BEM

To accommodate the implementation of the semi-analytical adjoint method for the estimation of the design sensitivities, it has been necessary to solve the viscothermal BEM equations differently compared to the previous implementations. Instead of relying on a series of Schur complement operations, we will here solve the Kirchhoff decomposition and the associated boundary conditions by formulating the fully coupled system of equations in Eq. (7). The system matrix $\mathbf{S}_{\mathrm{KD}}$ is defined as

$$\mathbf{S}_{\mathrm{KD}} = \begin{bmatrix} \mathbf{A}_a & -\mathbf{B}_a & \mathbf{0} & \mathbf{0} & \mathbf{0} & \mathbf{0} & \mathbf{0} & \mathbf{0} \\ \mathbf{0} & \mathbf{0} & \mathbf{A}_h & -\mathbf{B}_h & \mathbf{0} & \mathbf{0} & \mathbf{0} & \mathbf{0} \\ \tau_a \mathbf{I} & \mathbf{0} & \tau_h \mathbf{I} & \mathbf{0} & \mathbf{0} & \mathbf{0} & \mathbf{0} & \mathbf{0} \\ \mathbf{0} & \mathbf{0} & \mathbf{0} & \mathbf{0} & \mathbf{A}_v & -\mathbf{B}_v & \mathbf{0} & \mathbf{0} \\ \mathbf{0} & \mathbf{0} & \mathbf{0} & \mathbf{0} & \mathbf{0} & \mathbf{0} & \mathbf{A}_v & -\mathbf{B}_v \\ \mathbf{0} & \phi_a \mathbf{I} & \mathbf{0} & \phi_h \mathbf{I} & \mathrm{diag}\left(\mathbf{n}_r\right) & \mathbf{0} & \mathrm{diag}\left(\mathbf{n}_z\right) & \mathbf{0} \\ \phi_a \mathbf{D}_t & \mathbf{0} & \phi_h \mathbf{D}_t & \mathbf{0} & \mathrm{diag}\left(\mathbf{t}_r\right) & \mathbf{0} & \mathrm{diag}\left(\mathbf{t}_z\right) & \mathbf{0} \\ \mathbf{0} & \mathbf{0} & \mathbf{0} & \mathbf{0} & \left(\left(\mathbf{r} \circ \mathbf{t}_r\right) \mathbf{1}^{\mathrm{T}}\right) \circ \mathbf{D}_t & \mathrm{diag}\left(\mathbf{r} \circ \mathbf{n}_r\right) & \left(\left(\mathbf{r} \circ \mathbf{t}_r\right) \mathbf{1}^{\mathrm{T}}\right) \circ \mathbf{D}_t & \mathrm{diag}\left(\mathbf{r} \circ \mathbf{n}_z\right) \end{bmatrix} \tag{A.1}$$

In Eq. (A.1), $\mathbf{D}_t$ is a tangential derivative matrix based on the shape function derivative approach found in Ref. [37]. Moreover, $\mathbf{n}_r$, $\mathbf{n}_z$, $\mathbf{t}_r$ and $\mathbf{t}_z$ are the r and z components of the normal and tangential unit vectors n and t to Γ at the individual nodes. The operator $\mathrm{diag}(\mathbf{x})$ creates a matrix with the vector $\mathbf{x}$ in the diagonal. $\mathbf{r}$ is a vector with the r-coordinates of the nodes, $\mathbf{l}$ is a vector containing ones and $\circ$ is the Hadamard element-wise product.

The unknown variables and the right-hand side in Eq. (7) are

$$\mathbf{x} = \begin{bmatrix} \mathbf{p}_a \\ \frac{\partial \mathbf{p}_a}{\partial n} \\ \mathbf{p}_h \\ \frac{\partial \mathbf{p}_h}{\partial n} \\ \mathbf{v}_{v,r} \\ \frac{\partial \mathbf{v}_{v,r}}{\partial n} \\ \mathbf{v}_{v,z} \\ \frac{\partial \mathbf{v}_{v,z}}{\partial n} \end{bmatrix}, \quad \mathbf{f} = \begin{bmatrix} \mathbf{0} \\ \mathbf{0} \\ \mathbf{0} \\ \mathbf{0} \\ \mathbf{0} \\ \mathbf{v}_{b,n} \\ \mathbf{v}_{b,t} \\ \mathbf{0} \end{bmatrix}. \tag{A.2}$$

Solving the system in this expanded manner will allow for a simple way of evaluating the matrix derivative semi-analytically as described in Section 7.1.

Appendix B. In-depth development of semi-analytical adjoint sensitivities for the absorption coefficient

Both the KD-BEM and the BLI-BEM use a semi-analytical adjoint approach to evaluate the sensitivities. In the following, an in-depth derivation of the terms in Eqs. (17) and (18) are only given for the KD-BEM implementations, however, the same approach can be used for the BLI-BEM.

B.1. Obtaining $\frac{\partial \phi_0}{\partial \rho_i}$

The term $\frac{\partial \phi_0}{\partial \rho_i}$ for the KD-BEM is derived as follows,

$$\begin{aligned} \frac{\partial \phi_0}{\partial \rho_i} &= -\frac{\partial}{\partial \rho_i}\left(\left|e^{-\mathrm{i}k_{LL}d} - H\right|^2 \left|H - e^{\mathrm{i}k_{LL}d}\right|^{-2}\right) \\ &= -\left(\frac{\partial}{\partial \rho_i}\left(\left|e^{-\mathrm{i}k_{LL}d} - H\right|^2\right)\left|H - e^{\mathrm{i}k_{LL}d}\right|^{-2} \right. \\ &\quad \left. + \left|e^{-\mathrm{i}k_{LL}d} - H\right|^2 \frac{\partial}{\partial \rho_i}\left(\left|H - e^{\mathrm{i}k_{LL}d}\right|^{-2}\right)\right) \end{aligned} \tag{B.1}$$

where $H = \frac{p_2}{p_1}$. The first derivative term in Eq. (B.1) becomes,

$$\begin{aligned} \frac{\partial}{\partial \rho_i}\left(\left|e^{-\mathrm{i}k_{LL}d} - H\right|^2\right) = &-2\left|e^{-\mathrm{i}k_{LL}d} - H\right|\left(\Re(e^{-\mathrm{i}k_{LL}d} - H)^2 + \Im(e^{-\mathrm{i}k_{LL}d} - H)^2\right)^{-1/2} \\ &\left[\Re(e^{-\mathrm{i}k_{LL}d} - H)\frac{\partial \Re(H)}{\partial \rho_i} + \Im(e^{-\mathrm{i}k_{LL}d} - H)\frac{\partial \Im(H)}{\partial \rho_i}\right] \end{aligned} \tag{B.2}$$

where,

$$\begin{aligned} \frac{\partial \Re(H)}{\partial \rho_i} = &\left(\frac{\partial}{\partial \rho_i}\left(\left(p_{1,r}^2 + p_{1,i}^2\right)^{-1}\right)\right)\left(p_{2,r}p_{1,r} + p_{2,i}p_{1,i}\right) + \\ &\left(p_{1,r}^2 + p_{1,i}^2\right)^{-1}\left(\frac{\partial}{\partial \rho_i}\left(p_{2,r}p_{1,r} + p_{2,i}p_{1,i}\right)\right). \end{aligned} \tag{B.3}$$

The subscripts r and i are denoting the real and imaginary parts, respectively. The design derivatives in Eq. (B.3) can further be derived as

$$\frac{\partial}{\partial \rho_i}\left(\left(p_{1,r}^2 + p_{1,i}^2\right)^{-1}\right) = -\left(p_{1,r}^2 + p_{1,i}^2\right)^{-2}\left(2p_{1,r}\frac{\partial p_{1,r}}{\partial \rho_i} + 2p_{1,i}\frac{\partial p_{1,i}}{\partial \rho_i}\right) \tag{B.4}$$

and

$$\frac{\partial}{\partial \rho_i}\left(p_{2,r}p_{1,r} + p_{2,i}p_{1,i}\right) = \frac{\partial p_{2,r}}{\partial \rho_i}p_{1,r} + p_{2,r}\frac{\partial p_{1,r}}{\partial \rho_i} + \frac{\partial p_{2,i}}{\partial \rho_i}p_{1,i} + p_{2,i}\frac{\partial p_{1,i}}{\partial \rho_i}. \tag{B.5}$$

Hereafter, the field point derivatives of p_1 and p_2 are given by

$$\frac{\partial p_{p,r}}{\partial \rho_i} = \frac{\partial \mathbf{A}_{a,p,r}}{\partial \rho_i}\mathbf{p}_{a,r} - \frac{\partial \mathbf{A}_{a,p,i}}{\rho_i}\mathbf{p}_{a,i} - \left(\frac{\partial \mathbf{B}_{a,p,r}}{\partial \rho_i}\frac{\partial \mathbf{p}_{a,r}}{\partial n} - \frac{\partial \mathbf{B}_{a,p,i}}{\partial \rho_i}\frac{\partial \mathbf{p}_{a,i}}{\partial n}\right) \tag{B.6}$$

$$\frac{\partial p_{p,i}}{\partial \rho_i} = \frac{\partial \mathbf{A}_{a,p,r}}{\partial \rho_i}\mathbf{p}_{a,i} + \frac{\partial \mathbf{A}_{a,p,i}}{\partial \rho_i}\mathbf{p}_{a,r} - \left(\frac{\partial \mathbf{B}_{a,p,r}}{\partial \rho_i}\frac{\partial \mathbf{p}_{a,i}}{\partial n} + \frac{\partial \mathbf{B}_{a,p,i}}{\partial \rho_i}\frac{\partial \mathbf{p}_{a,r}}{\partial n}\right) \tag{B.7}$$

where the subscript p is denoting the specific field point (either $p = 1$ or $P = 2$). The field point derivative matrices can hereafter be evaluated semi-analytically. It should be noted that this approach disregards the contribution from the thermal pressure when evaluating the field points. This is however a fair assumption since the contribution from the thermal pressure is negligible inside the impedance tube and away from boundaries at p_1 and p_2. The term $\frac{\partial \Im(H)}{\partial \rho_i}$ can be evaluated using a similar derivation. Further, the second derivative term in Eq. (B.1) becomes,

$$\begin{aligned}\frac{\partial}{\partial \rho_i}\left(\left|H - e^{\mathrm{i}k_{LL}d}\right|^{-2}\right) =& -2\left|H - e^{\mathrm{i}k_{LL}d}\right|^{-3}\left(H - e^{\mathrm{i}k_{LL}d}\right)^{-1/2}\\ &\left[\Re(H - e^{\mathrm{i}k_{LL}d})\frac{\partial \Re(H)}{\partial \rho_i} + \Im(H - e^{\mathrm{i}k_{LL}d})\frac{\partial \Im(H)}{\partial \rho_i}\right]\end{aligned} \tag{B.8}$$

B.2. Obtaining $\frac{\partial \phi_0}{\partial \mathbf{x}_r}$

The term $\frac{\partial \phi_0}{\partial \mathbf{x}_r}$ in Eq. (18) is derived as follows,

$$\begin{aligned}\frac{\partial \phi_0}{\partial \mathbf{x}_r} =& -\left(\frac{\partial}{\partial \mathbf{x}_r}\left(\left|e^{-\mathrm{i}k_{LL}d} - H\right|^2\right)\left|H - e^{\mathrm{i}k_{LL}d}\right|^{-2}\right.\\ &\left.+\left|e^{-\mathrm{i}k_{LL}d} - H\right|^2\frac{\partial}{\partial \mathbf{x}_r}\left(\left|H - e^{\mathrm{i}k_{LL}d}\right|^{-2}\right)\right)\end{aligned} \tag{B.9}$$

where the first derivative term is given as

$$\begin{aligned}\frac{\partial}{\partial \mathbf{x}_r}\left(\left|e^{-\mathrm{i}k_{LL}d} - H\right|^2\right) =& -2\left|e^{-\mathrm{i}k_{LL}d} - H\right|\left(\Re(e^{-\mathrm{i}k_{LL}d} - H)^2 + \Im(e^{-\mathrm{i}k_{LL}d} - H)^2\right)^{-1/2}\\ &\left[\Re(e^{-\mathrm{i}k_{LL}d} - H)\frac{\partial \Re(H)}{\partial \mathbf{x}_r} + \Im(e^{-\mathrm{i}k_{LL}d} - H)\frac{\partial \Im(H)}{\partial \mathbf{x}_r}\right].\end{aligned} \tag{B.10}$$

Now it is a matter of evaluating $\frac{\partial \Re(H)}{\partial \mathbf{x}_r}$ and $\frac{\partial \Im(H)}{\partial \mathbf{x}_r}$. Their evaluation is very similar. Therefore, the following derivation will limit itself to the development of $\frac{\partial \Re(H)}{\partial \mathbf{x}_r}$

$$\begin{aligned}\frac{\partial \Re(H)}{\partial \mathbf{x}_r} =& \left(\frac{\partial}{\partial \mathbf{x}_r}\left(p_{1,r}^2 + p_{1,i}^2\right)^{-1}\right)\left(p_{2,r}p_{1,r} + p_{2,i}p_{1,i}\right) +\\ &\left(p_{1,r}^2 + p_{1,i}^2\right)^{-1}\left(\frac{\partial}{\partial \mathbf{x}_r}\left(p_{2,r}p_{1,r} + p_{2,i}p_{1,i}\right)\right)\end{aligned} \tag{B.11}$$

with

$$\frac{\partial}{\partial \mathbf{x}_r}\left(p_{1,r}^2 + p_{1,i}^2\right)^{-1} = -\left(p_{1,r}^2 + p_{1,i}^2\right)^{-2}\left(2p_{1,r}\frac{\partial p_{1,r}}{\partial \mathbf{x}_r} + 2p_{1,i}\frac{\partial p_{1,i}}{\partial \mathbf{x}_r}\right) \tag{B.12}$$

and

$$\frac{\partial}{\partial \mathbf{x}_r}\left(p_{2,r}p_{1,r} + p_{2,i}p_{1,i}\right) = \frac{\partial p_{2,r}}{\partial \mathbf{x}_r}p_{1,r} + p_{2,r}\frac{\partial p_{1,r}}{\partial \mathbf{x}_r} + \frac{\partial p_{2,i}}{\partial \mathbf{x}_r}p_{1,i} + p_{2,i}\frac{\partial p_{1,i}}{\partial \mathbf{x}_r} \tag{B.13}$$

where field point pressure derivatives are obtained as

$$\left(\frac{\partial p_{p,r}}{\partial \mathbf{x}_r}\right)^{\mathrm{T}} = \begin{bmatrix}\left(\mathbf{A}_{a,p,r}\right)^{\mathrm{T}}\\ \left(-\mathbf{B}_{a,p,r}\right)^{\mathrm{T}}\\ \mathbf{0}\\ \mathbf{0}\\ \mathbf{0}\\ \mathbf{0}\\ \mathbf{0}\\ \mathbf{0}\end{bmatrix} \quad \text{and} \quad \left(\frac{\partial p_{p,i}}{\partial \mathbf{x}_r}\right)^{\mathrm{T}} = \begin{bmatrix}\left(\mathbf{A}_{a,p,i}\right)^{\mathrm{T}}\\ \left(-\mathbf{B}_{a,p,i}\right)^{\mathrm{T}}\\ \mathbf{0}\\ \mathbf{0}\\ \mathbf{0}\\ \mathbf{0}\\ \mathbf{0}\\ \mathbf{0}\end{bmatrix} \tag{B.14}$$

Continuing with the second derivative term in Eq. (B.9), we obtain

$$\begin{aligned}\frac{\partial}{\partial \mathbf{x}_r}\left(\left|H - e^{\mathrm{i}k_{LL}d}\right|^{-2}\right) =& -2\left|H - e^{\mathrm{i}k_{LL}d}\right|^{-3}\left(H - e^{\mathrm{i}k_{LL}d}\right)^{-1/2}\\ &\left[\Re(H - e^{\mathrm{i}k_{LL}d})\frac{\partial \Re(H)}{\partial \mathbf{x}_r} + \Im(H - e^{\mathrm{i}k_{LL}d})\frac{\partial \Im(H)}{\partial \mathbf{x}_r}\right]\end{aligned} \tag{B.15}$$

Obtaining $\frac{\partial \phi_0}{\partial \mathbf{x}_i}$ is very similar to the approach presented here. Therefore, the development will not be repeated.

References

[1] G. Kirchhoff, Uber den einfluss der wärmeleitung in einem gase auf due SchallBewegung, Ann. Phys. Chem. 210 (6) (1868) 177–193, http://dx.doi.org/10.1002/andp.18682100602, English translation: "On the influence of thermal conduction in a gas in sound propagation".

[2] Rayleigh, The Theory of Sound Vol. 2, second ed., Dover Publications, New York, United States of America, 1894.

[3] W.R. Kampinga, Viscothermal Acoustics Using Finite Elements. Analysis Tool for Engineers (Ph.D. thesis), University of Twente, Enschede, 2010.

[4] R. Christensen, Acoustic Modeling of Hearing Aid Components (Ph.D. thesis), University of Southern Denmark, 2010.

[5] V. Cutanda Henríquez, Numerical Transducer Modeling (Ph.D. thesis), Technical University of Denmark, Lyngby, 2002.

[6] D. Homentcovschi, R.N. Miles, P.V. Loeppert, A.J. Zuckerwar, A microacoustic analysis including viscosity and thermal conductivity to model the effect of the protective cap on the acoustic response of a mems microphone, Microsyst. Technol.-Micro Nanosyst.-Inf. Storage Process. Syst. 20 (2) (2014) 265–272, http://dx.doi.org/10.1007/s00542-013-1800-5.

[7] S.B. Dilgen, Topology and Advanced Shape Optimization of Multiphysics Problems (Ph.D Thesis), Technical University of Denmark, 2020.

[8] E. Creixell Mediante, Computational Reduction Techniques for Numerical Vibro-Acoustic Analysis of Hearing Aids (Ph.D Thesis), Technical University of Denmark, Department of Electrical Engineering, 2018.

[9] V. Cutanda Henríquez, V.M. García-Chocano, J. Sánchez-Dehesa, Viscothermal losses in double-negative acoustic metamaterials, Phys. Rev. Appl. 8 (2017) 014029, http://dx.doi.org/10.1103/PhysRevApplied.8.014029, URL https://link.aps.org/doi/10.1103/PhysRevApplied.8.014029.

[10] M. Molerón, M. Serra-Garcia, C. Daraio, Visco-thermal effects in acoustic metamaterials: from total transmission to total reflection and high absorption, New J. Phys. 18 (2016) 033003, http://dx.doi.org/10.1088/1367-2630/18/3/033003.

[11] J. Carbajo, J. Ramis, L. Godinho, P. Amado-Mendes, J. Alba, A finite element model of perforated panel absorbers including viscothermal effects, Appl. Acoust. 90 (2015) 1–8, http://dx.doi.org/10.1016/j.apacoust.2014.10.013.

[12] M. Bruneau, P. Herzog, J. Kergomard, J.D. Polak, General formulation of the dispersion equation in bounded viso-thermal fluid, and application to some simple geometries, Wave Motion 11 (1988) 441–451, http://dx.doi.org/10.1016/j.jcp.2006.09.018.

[13] V. Cutanda Henríquez, P.M. Juhl, An axisymmetric boundary element formulation of sound wave propagation in fluids including viscous and thermal losses, J. Acoust. Soc. 134 (5) (2013) 3409–3418, http://dx.doi.org/10.1121/1.4823840.

[14] P.R. Andersen, V. Cutanda Henríquez, N. Aage, Shape optimization of micro-acoustic devices including viscous and thermal losses, J. Sound Vib. 447 (2019) 120–136, http://dx.doi.org/10.1016/j.jsv.2019.01.047.

[15] M.J.J. Nijhof, Y.H. Wijant, A. de Boer, An acoustic finite element including viscothermal effects, in: Proceedings from the 14th International Congress on Sound and Vibration, 9-12 July, Cairns (Australia), 2007.

[16] M. Berggren, A. Bernland, D. Noreland, Acoustic boundary layers as boundary conditions, J. Comput. Phys. 371 (2018) 633–650, http://dx.doi.org/10.1016/j.jcp.2018.06.005.

[17] M.J. Cops, J.G. McDaniel, E.A. Magliula, D.J. Bamford, M. Berggren, Estimation of acoustic absorption in porous materials based on visco-thermal boundary layers modeled as boundary conditions, J. Acoust. Soc. 148 (3) (2020) 1624–1635, http://dx.doi.org/10.1121/10.0001959.

[18] G. Tissot, R. Billard, G. Gabard, Optimal cavity shape design for acoustic liners using Helmholtz equation with visco-thermal losses, J. Comput. Phys. 402 (2020) 109048, http://dx.doi.org/10.1016/j.jcp.2019.109048.

[19] J. Jith, S. Sarkar, Boundary layer impedance model to analyse the visco-thermal acousto-elastic interactions in centrifugal compressors, J. Fluids Struct. 81 (2018) 179–200, http://dx.doi.org/10.1016/j.jfluidstructs.2018.05.002.

[20] COMSOL Multiphysics Acoustics Module User's Guide, version 5.6, COMSOL, Inc, p. 110, www.comsol.com.

[21] R. Billard, G. Tissot, G. Gabard, M. Versaevel, Numerical simulations of perforated plate liners: Analysis of the visco-thermal dissipation mechanisms, J. Acoust. Soc. 149 (1) (2021) 16–27, http://dx.doi.org/10.1121/10.0002973.

[22] R. Udawalpola, M. Berggren, Optimization of an acoustic horn with respect to efficiency and directivity, Int. J. Numer. Methods Eng. 73 (11) (2008) 1571–1606, http://dx.doi.org/10.1002/nme.2132.

[23] R. Udawalpola, E. Wadbro, M. Berggren, Optimization of a variable mouth acoustic horn, Int. J. Numer. Methods Eng. 85 (5) (2011) 591–606, http://dx.doi.org/10.1002/nme.2982.

[24] H. Dong, Y. Shen, H. Gao, Shape optimization of acoustic horns using the multimodal method, J. Acoust. Soc. 147 (4) (2020) EL326–EL332, http://dx.doi.org/10.1121/10.0001037.

[25] R. Christensen, Shape and topology optimization of loudspeaker drivers, in: Proceedings of the COMSOL Conference 2020 (Grenoble/Online), 2020.

[26] A. Bezzola, Numerical optimization strategies for acoustic elements in loudspeaker design, in: 145th Audio Engineering Society International Convention, AES, New York, United States of America, 2018.

[27] A. Bernland, E. Wadbro, M. Berggren, Shape optimization of a compression driver phase plug, SIAM J. Sci. Comput. 41 (1) (2019) B181–B204, http://dx.doi.org/10.1137/18M1175768.

[28] F. Jiang, W. Zhao, L. Chen, C. Zheng, H. Chen, Combined shape and topology optimization for sound barrier by using the isogeometric boundary element method, Eng. Anal. Bound. Elem. 124 (2021) 124–136, http://dx.doi.org/10.1016/j.enganabound.2020.12.009.

[29] C. Liu, L. Chen, W. Zhao, H. Chen, Shape optimization of sound barrier using an isogeometric fast multipole boundary element method in two dimensions, Eng. Anal. Bound. Elem. 85 (2017) 142–157, http://dx.doi.org/10.1016/j.enganabound.2017.09.009.

[30] C.B. Dilgen, N. Aage, Generalized shape optimization of transient vibroacoustic problems using cut elements, Int. J. Numer. Methods Eng. 122 (6) (2021) 1578–1601, http://dx.doi.org/10.1002/nme.6591.

[31] M.B. Dühring, J.S. Jensen, O. Sigmund, Acoustic design by topology optimization, J. Sound Vib. 317 (2008) 557–575.

[32] C.B. Dilgen, S.B. Dilgen, N. Aage, J.S. Jensen, Topology optimization of acoustic mechanical interaction problems: a comparative review, Struct. Multidiscip. Optim. 60 (2) (2019) 779–801, http://dx.doi.org/10.1007/s00158-019-02236-4.

[33] P.M. Juhl, The Boundary Element Method for sound Field Calculations (Ph.D. thesis), Department of Acoustic Technology, Technical Univarity of Denmark, 1993.

[34] V. Cutanda Henríquez, P. Juhl, F. Jacobsen, On the modeling of narrow gaps using the standard BEM, J. Acoust. Soc. 109 (4) (2001) 1296–1303, http://dx.doi.org/10.1121/1.1350399.

[35] R.B. Lindsay, Acoustics: An introduction to its physical principles and applications, by Allan D. Pierce, J. Acoust. Soc. 70 (5) (1981) 1548, http://dx.doi.org/10.1121/1.387085.

[36] P. Morse, K. Ingard, Theoretical Acoustics, McGraw-Hill, New York, United States of America, 1968, p. 927.

[37] V. Cutanda Henríquez, A. Risby Andersen, A three-dimensional acoustic boundary element method formulation with viscous and thermal losses based on shape function derivatives, J. Theor. Comput. Acoust. 26 (2018) 1850039, http://dx.doi.org/10.1142/S2591728518500391.

[38] ISO 10534-2:1998, Acoustics – Determination of Sound Absorption Coefficient and Impedance in Impedance Tubes – Part 2: Transfer-Function Method, Standard, International Organization for Standardization, 1998.

[39] P.R. Johnston, C2-continuous elements for boundary element analysis, Int. J. Numer. Methods Eng. 40 (11) (1997) 2087–2108.

[40] L. Chen, C. Zheng, H. Chen, A wideband FMBEM for 2D acoustic design sensitivity analysis based on direct differentiation method, Comput. Mech. 52 (3) (2013) 631–648, http://dx.doi.org/10.1007/s00466-013-0836-9.

[41] T. Matsumoto, T. Yamada, T. Takahashi, C.J. Zheng, S. Harada, Acoustic design shape and topology sensitivity formulations based on adjoint method and BEM, Comput. Model. Eng. Sci. 78 (2) (2011) 77–94.
[42] L. Chen, L. Liu, W. Zhao, H. Chen, 2D acoustic design sensitivity analysis based on adjoint variable method using different types of boundary elements, Acoust. Aust. 44 (2) (2016) 343–357, http://dx.doi.org/10.1007/s40857-016-0065-4.
[43] P.R. Andersen, J. Kook, V. Cutanda Henríquez, N. Aage, Towards large-scale acoustic shape optimization for industrial applications using the boundary element method, in: Proceedings Internoise 2020, Seoul, South Korea, International Institute of Noise Control Engineering, 2020.
[44] L. Cremer, H.A. Müller, Principles and Applications of Room Acoustics Vol. 2, Applied Science Publishers, Ltd., Barkiny, Essex, England, 1982.
[45] N. Jiménez, V. Romero-García, V. Pagneux, J.P. Groby, Rainbow-trapping absorbers: Broadband, perfect and asymmetric sound absorption by subwavelength panels for transmission problems, Science 7 (1) (2017) 13595, http://dx.doi.org/10.1038/s41598-017-13706-4.
[46] S. Huang, X. Fang, X. Wang, B. Assouar, Q. Cheng, Y. Li, Acoustic perfect absorbers via Helmholtz resonators with embedded apertures, J. Acoust. Soc. 145 (1) (2019) 254–262, http://dx.doi.org/10.1121/1.5087128.
[47] V. Romero-García, N. Jiménez, G. Theocharis, V. Achilleos, A. Merkel, O. Richoux, V. Tournat, J.P. Groby, V. Pagneux, Design of acoustic metamaterials made of Helmholtz resonators for perfect absorption by using the complex frequency plane, C. R. Phys. 21 (7–8) (2021) 713–749, http://dx.doi.org/10.5802/CRPHYS.32.
[48] D.Y. Maa, Potential of microperforated panel absorber, J. Acoust. Soc. 104 (5) (1998) 2861–2866, http://dx.doi.org/10.1121/1.423870.
[49] M.A. Temiz, J. Tournadre, I.L. Arteaga, A. Hirschberg, Non-linear acoustic transfer impedance of micro-perforated plates with circular orifices, J. Sound Vib. 366 (2016) 418–428, http://dx.doi.org/10.1016/j.jsv.2015.12.022.
[50] M. Peters, A. Hirschberg, Acoustically induced periodic vortex shedding at sharp edged open channel ends - simple vortex models, J. Sound Vib. 161 (2) (1993) 281–299, http://dx.doi.org/10.1006/jsvi.1993.1072.